Materials and Interfaces

Scilight

Article

Controlled Polymerization of Aniline against Templating Oxide Nanostructures

Matas Simukaitis [1], Grace Purnell [1], Zachary Zander [2], Danielle Kuhn [2], and Yugang Sun [1,*]

[1] Department of Chemistry, Temple University, 1901 North 13th Street, Philadelphia, PA 19122, USA
[2] U.S. Army DEVCOM Chemical Biological Center, Research & Technology Directorate, Aberdeen Proving Ground, MD 21010, USA
* Correspondence: ygsun@temple.edu

Received: 6 November 2024; Revised: 30 November 2024; Accepted: 3 December 2024; Published: 4 December 2024

Abstract: Conducting polyaniline (PANI) nanotubes with strong broadband optical absorption have been synthesized using single-crystalline MnO_2 nanotubes as a solid-state oxidant that can oxidize aniline to induce polymerization in acidic solutions. The smooth surfaces and high crystalline integrity of the MnO_2 nanotubes provide the appropriate reactive solid/liquid interface and templating effect to enable the transformation of the MnO_2 nanotubes into PANI nanotubes. Such templated chemical transformation can be extended to silica-coated MnO_2 nanotubes, allowing the synthesis of silica-coated PANI nanotubes, which are challenging to be synthesized through direct coating silica on PANI nanotubes due to the low wettability between PANI and silica. The versatile chemistry of the outer silica shells opens the possibility of modifying the as-synthesized PANI nanotubes, which usually inconveniently graft other interesting motifs.

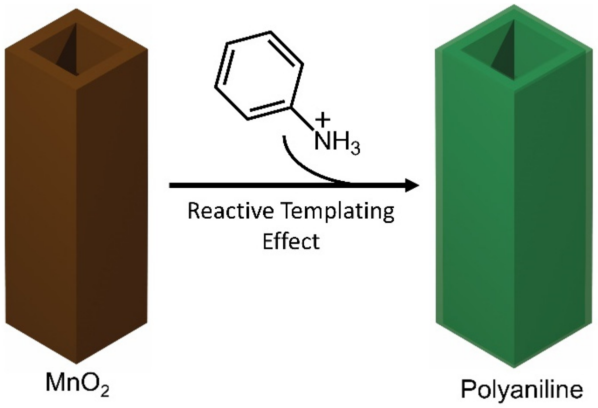

Keywords: templated redox reaction synthesis; conducting polymer nanotubes; inorganic-polymer core-shell nanotubes; broadband optical absorption composite nanomaterials

1. Introduction

Polyaniline (PANI), a widely studied conducting polymer, has shown great promise in many fields, such as sensing, energy storage, and medicine, owing to its favorable physical properties, tunable electrical conductivity, ease of processing, and stability [1–5]. While polymerization of aniline monomer is a simple process initiated in the presence of an appropriate oxidant [6,7], shape-controlled synthesis of PANI nanostructures is still challenging. For example, the widely adopted approach is using ammonium persulfate (APS), a soluble oxidant salt with a redox potential of 2.01 V (*vs*. SHE or standard hydrogen electrode), to enable the polymerization of aniline (with a redox potential of 1.10 V) [8]. Persulfate ions oxidize aniline monomer rapidly in solution, leading to difficulty in controlling the morphology of PANI. Emerging strategies for controlling the shape of PANI nanostructures include confined polymerization in micelles [9,10], self-assembly micro/nanotubes [11], and polymerization on inert nanoparticle surfaces followed by post-processing [12]. Alternatively, a solid-state oxidant that relies on the exposed surface to react with aniline could provide controllability over reaction kinetics to enable a controlled growth of PANI nanostructures. When the solid-state oxidant is a nanostructure with a desirable shape, it oxidizes aniline to initiate a polymerization reaction, forming a PANI nanoparticle with a shape determined by the oxidant nanostructure. The solid-state oxidant nanostructure provides the important solid-liquid interface to restrict the reaction kinetics and confine the polymerization adjacent to the nanostructure surface, in which the oxidant nanostructure behaves as a reactive transient template. For instance, nanostructures of manganese oxides [13–19] and cerium dioxides (ceria) [20] have been reported to react with aniline and guide polymerization of aniline, forming PANI nanostructures with inheritance of the geometries of the oxide nanostructures. Reproducing the reported recipes showed that some oxide nanostructures (e.g., MnO_2 nanorods and nanotubes) gave successful production of PANI nanostructures with controlled shapes, but some oxide nanostructures (e.g., ceria nanoparticles, MnO_2 flowers, MnO_2 spheres) failed to produce the well-shaped PANI nanostructures. Such inconsistent reproducibility motivated us to investigate the critical parameters of the oxide nanostructures to determine the success of producing well-shaped PANI nanostructures.

In this work, we compare the use of CeO_2 nanoparticles, desert rose-like δ-MnO_2 flowers, and single-crystalline α-MnO_2 nanotubes in reaction with aniline and analyze whether the geometries of the oxide nanostructures are preserved in the resulting PANI nanostructures. Conducting PANI nanotubes are successfully synthesized by using the α-MnO_2 nanotubes as the reactive template to oxidize aniline and facilitate polymerization reaction in a controlled manner, without the appearance of randomly formed PANI. The standard reduction potential of MnO_2/Mn^{2+} pair is 1.23 V, which is high enough to oxidize aniline under appropriate conditions, for example, a high acidity of the reaction solution that allows the solid MnO_2 is reduced to soluble Mn^{2+} ions. Reducing MnO_2 nanotubes to soluble ions is essential to continuously expose reactive MnO_2 surfaces to oxidize aniline and drive polymerization reaction. In addition, the single crystallinity of the MnO_2 nanotubes prevents them from being shattered during the redox reaction, facilitating the formation of PANI nanotubes due to the templating effect. In contrast, the polycrystalline δ-MnO_2 flowers made of intertwined thin nanoflakes and polycrystalline $MnCO_3$@MnO_2 spherical particles with rough surfaces react with aniline to form entangled PANI nanofibers without inheriting the MnO_2 geometries. The stark difference indicates that high crystallinity and smooth surfaces of the reactive template oxide nanostructures are crucial to forming integral PANI nanostructures with the preservation of oxide geometries. The evolution of PANI nanotubes has been examined to understand the shape preservation of the single-crystalline MnO_2 nanotubes during the templated redox reaction.

2. Materials and Methods

2.1. Synthesis of MnO_2 Nanotubes

Single-crystalline MnO_2 nanotubes were synthesized through a hydrothermal method. In a typical synthesis, 112.5 mg of $KMnO_4$ (Acros Organics, ACS Reagent, 99%+, Fair Lawn, NJ, USA) was dissolved in 10 mL of DI H_2O. To this solution was added 0.250 mL of concentrated HCl (Fisher Chemical, ACS Plus Reagent, 37% *w*/*w*, Fair Lawn, NJ, USA) under magnetic stirring, and the solution was allowed to stir for 30 min. The solution was transferred to a Teflon-lined stainless steel hydrothermal reactor, which was then placed in an oven set at 120 °C for 12 h. The reactor was allowed to cool completely to room temperature before opening. The solid product was washed three times with DI H_2O and one time with ethanol (Pharmco, 190 proof, Brookfield, CT, USA) before drying in an oven set at 60 °C overnight.

2.2. Synthesis of PANI Nanotubes

In a synthesis, 15 mg of the as-prepared MnO_2 nanotubes were dispersed in 5 mL of DI H_2O. To this dispersion was added 0.2 mL of 0.6 M H_2SO_4 (Fisher Chemical, Certified ACS Plus, 95% *w*/*w*, Fair Lawn, NJ, USA). The dispersion was ultrasonicated for 30 min. A separate solution containing 18 mL of aniline (Acros Organics, ACS Reagent, 99%, Fair Lawn, NJ, USA) in 1 mL of DI H_2O was prepared. Following the 30-min ultrasonication period, the aniline solution was added to the dispersion of MnO_2 nanotubes to trigger the redox and polymerization reactions. The reaction was performed at room temperature and ambient air atmosphere. The PANI product was washed three times with DI H_2O before being dispersed in 5 mL of ethanol for storage.

2.3. Synthesis of PANI@silica Nanotubes

The as-synthesized MnO_2 nanotubes were first coated with silica with an appropriate thickness through a sol-gel process. For example, 15 mg of MnO_2 nanotubes were dispersed in a solution containing 2.5 mL DI H_2O and 0.5 mL NH_4OH with the assistance of ultrasonication. While magnetic stirring, to the MnO_2 dispersion 12 mL of 0.03 M cetyltrimethylammonium bromide (CTAB) (CHEM-IMPEX INT'L INC., 99.52%, Wood Dale, IL, USA) solution in H_2O/ethanol (*v*/*v* = 2:1) was added dropwise and the magnetical stirring continued for additional 30 min. A solution containing the appropriate amount of tetraethyl orthosilicate (TEOS) (Acros Organics, 98%, Fair Lawn, NJ, USA) in 0.5 mL of pure ethanol was then added dropwise to the dispersion, followed with continuous stirring at room temperature overnight. The solution was centrifuged and washed with DI H_2O and ethanol to remove excess CTAB. The MnO_2@silica nanotubes were dried in an oven set at 60 °C before use. Transforming the MnO_2 nanotubes to PANI nanotubes inside the silica coating followed the same procedure described above.

2.4. XRD Characterization

The XRD characterization was performed using a Bruker D8 Advance diffractometer (Billerica, MA, USA). The as-synthesized MnO_2 product powder was loaded to a sample holder made of Poly(Methyl Mathacrylate) (PMMA). The X-ray beam was generated using Cu K_a emission with wavelength of 1.5418 Å. The total power of the instrument was set at 1600 W. The measurement was recorded at a rate of 1 s per increment of 0.0204°.

2.5. TEM Characterization

The transmission electron microscopy (TEM) images were recorded using a JEOL JEM-1400 electron microscope equipped with a LaB_6 filament (Tokyo, Japan). For sample preparation, the PANI dispersion in ethanol was diluted by a factor of 4 with additional ethanol before a 20-μL aliquot was drop cast on a Formvar/carbon 200 mesh copper TEM grid (Ted Pella Inc. Redding, CA, USA). The solvent vaporized in a fume hood to dry the sample. All images were collected at an accelerating voltage of 120 kV with the beam current between 85–100 μA.

2.6. SEM/EDS Characterization

The scanning electron microscopy (SEM) images were recorded using a FEI Quanta 450FEG electron microscope (Hillsboro, OR, USA), which was equipped with an Oxford Instruents X-Max^N 50 detector for energy dispersive x-ray spectroscopy (EDS) characterization (High Wycombe, UK). For sample preparation, the PANI dispersion in ethanol was directly used and a 20-μL aliquot was drop-cast on a silicon chip. The solvent vaporized in a fume hood to dry the sample. All images were collected at an accelerating voltage of 10 kV. All EDS characterization and analysis was conducted using the AZtec software (Oxford Instruments, High Wycombe, UK).

2.7. UV-Visible Absorption/Extinction Spectroscopy

The UV-visible optical absorption/extinction spectroscopy was studied using a Thermo Scientific Evolution 220 UV-Visible spectrophotometer (Madison, WI, USA). For the study of reaction evolution, a 0.1-mL aliquot of the reaction solution was sampled at a specific time and dispersed in 1 mL of DI H_2O. The quartz cuvette was rinsed twice with DI H_2O between samples. The spectral scans were conducted at a rate of 3000 nm/min with an integration time of 30 milliseconds and a scan interval of 1.5 nm.

3. Results and Discussion

When a MnO_2 nanotube is immersed in acidic aniline solution, aniline molecules are in direct contact with the outer side surfaces and end surfaces of the nanotube to react and initiate polymerization to form a thin PANI layer on these surfaces (step i, Figure 1). Because of the small diameter of the nanotube, the diffusion of aniline into the tube cavity is significantly restricted, making it difficult to form a PANI layer against the inner surfaces of the MnO_2 nanotube. The thin PANI layer is still permeable to aniline monomer, allowing the continuous redox reaction between aniline and MnO_2 to grow the PANI layer. The outer side surfaces of the single-crystalline α-MnO_2 nanotube are smooth and terminated by the low-index {100} facets, while its end surfaces are rough (or curved) and terminated by the higher-index facets [21]. The crystallographic differences between the side and end surfaces lead to different reactivity: the end surfaces are more reactive than the outer side surfaces. As a result, the continuous reaction will consume MnO_2 along the longitudinal direction faster than the transverse direction. Such anisotropic reactivity results in a PANI nanotube with a shortened MnO_2 nanotube in the middle (step ii, Figure 1). The end portions of the PANI nanotube (with complete consumption of MnO_2) become thicker to reach the thickness determined by the reaction stoichiometry. Meanwhile, the PANI layer outside the remaining MnO_2 also slightly thickens even though the reaction along the transverse direction is slow. The further reaction will ultimately consume the MnO_2 nanotube to form a pure PANI nanotube with uniform thickness (step iii, Figure 1). The redox reaction and polymerization occurring against the MnO_2 surfaces ensures the resulting PANI to adopt the tubular morphology of the MnO_2 nanotube.

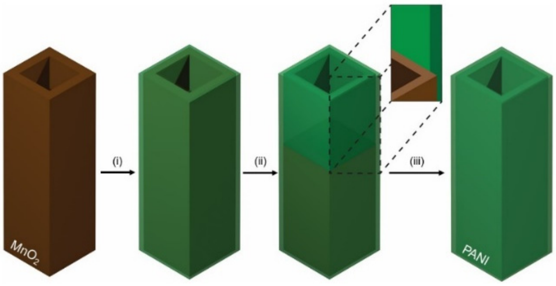

Figure 1. Schematic illustration of the major steps involved in the evolution of single-crystalline α-MnO_2 nanotube during the reaction with aniline, which results in a PANI nanotube.

PANI exists in three oxidation states: fully reduced leucoemeraldine, fully oxidized pernigraniline, and partially oxidized emeraldine phase. The former two forms exhibit negligible electric conductivity, while the latter emeraldine phase is highly conductive and represents the most studied PANI phase [7]. The conductivity and optical properties of PANI can be modulated by the concentration of doped protons along the polymer backbone, allowing delocalization of the trapped electron states. Therefore, strong acidity (or low pH) of reaction solutions is necessary to synthesize highly conductive PANI nanostructures. The polymerization reaction using APS yields H_2SO_4 as a byproduct, providing sufficient proton dopant to produce conductive PANI. In contrast, the polymerization reaction with MnO_2 consumes protons (Figure S1, ESI), preventing the formation of the conductive emeraldine phase. A high concentration of acid must be added to the reaction solution to maintain a sufficiently acidic condition for producing conductive PANI when using MnO_2 as a solid-state oxidant.

Single-crystalline α-MnO_2 nanotubes were synthesized using a hydrothermal method reported elsewhere [22]. The X-ray diffraction (XRD) pattern exhibits only a group of peaks consistent with the α-phase of MnO_2 (Figure S2). The electron microscopy images show their tubular geometry with smooth surfaces and square cross-sections. Each nanotube is straight with a uniform lateral dimension of 105 nm on average (Figure S3). In a typical reaction with aniline, 15 mg of the synthesized MnO_2 nanotubes were dispersed in 5 mL of deionized (DI) H_2O under ultrasonication. The pH of the aqueous dispersion was adjusted using 0.5 M H_2SO_4 aqueous solution to a value of 1.5 (or any value below 1.5, condition optimization in Table S1, ESI). A mixture of 0.013 mL of aniline and 1 mL of DI H_2O was then added to the acidified dispersion of MnO_2 nanotubes under vigorous magnetic stirring. The mixing promoted the redox reaction between aniline and the MnO_2 nanotubes, producing aniline radicals followed by polymerization into PANI. The dispersion was under constant stirring at room temperature to complete the reaction. Centrifuging the dispersion collects the PANI product, which was washed three times with DI H_2O and then dispersed in ethanol for further use.

The morphological and compositional evolution of the MnO_2 nanotubes during reaction with aniline in the acidic solution was studied by sampling the reaction solution at different times. The solid nanostructures in each aliquot were immediately collected through centrifugation and washing with DI H_2O. Figure 2 compares the TEM images of the typical individual nanotubes sampled at different reaction times. Each α-MnO_2 nanotube exhibits smooth side surfaces, open ends with curved end surfaces, and slightly tapered walls at the ends (Figure 2a). The line-scan energy-dispersive X-ray spectroscopy (EDS) across the nanotube shows a typical bell-curve profile of Mn with the presence of C that is common due to environment contamination (Figure 3a). The larger surface curvatures of the end surfaces are responsible for the higher reactivity than the side surfaces. The initial reaction of the MnO_2 nanotubes with aniline (i.e., for 1 min) formed a thin layer of PANI covering both the outer side surfaces and the end surfaces of the MnO_2 nanotubes (Figure 2b). The line scan EDS across the nanotube for both Mn and C exhibit the same profile with an increase of C signal relative to Mn (Figure 3b), confirming the occurrence of redox reaction that consumes MnO_2 and produces PANI. The PANI on the end surfaces is much thicker than on the side surfaces, which could be partially attributed to the different reactivity of the MnO_2 surfaces at different locations. In addition, the diffusion of aniline to the MnO_2 surfaces influences the redox reaction kinetics at the solid/liquid interface. The diffusion cross section for the end MnO_2 surfaces, which is close to a three-dimensional (3D) point diffusion model, is much larger than that for the side MnO_2 surfaces, which is equivalent to a two-dimension (2D) planar diffusion model (dashed curve vs. dashed line, Figure 2b). The difference in diffusion also contribute to the fast reaction on the end surfaces of the MnO_2 nanotubes, leading to the anisotropic shrink of the MnO_2 nanotubes along their longitudinal direction. Continuous reaction for 5 min shortens the MnO_2 nanotubes, forming composite nanotubes with multiple segments–pure PANI for the end sections and PANI/MnO_2 for the central section (Figure 2c). The compositional difference at different segments is evaluated with the line-scan EDS analysis (Figure 3c). The line-scan EDS profiles for both C and Mn at the central section are similar, confirming the incomplete consumption of MnO_2. The C intensity relative to Mn increases compared to the sample formed at 1 min, indicating that the redox reaction on the side surfaces of the MnO_2 nanotubes (i.e., along the transverse direction) still occurs, although the reaction rate is slower than that along the longitudinal direction. Another possibility of the redox reaction could be similar to the formation of hollow metal nanoparticles through the galvanic replacement reaction of silver nanoparticles with chloroauric acid [23]. Aniline molecules give out electrons on the outer surface, being oxidized to polymerize and thicken the PANI shells. The electrons migrate across the conductive PANI layer to inject into the MnO_2 nanotubes, reducing MnO_2 into soluble Mn^{2+} ions. In contrast, the line-scan EDS profiles at the end section show the absence of Mn, indicating that MnO_2 is completely consumed, and this section is composed of pure PANI. The apparent diameter of the end section is ~75% of that of the central section, implying the mechanical flexibility of the PANI nanotube. Without the support of the rigid MnO_2 nanotube, the PANI nanotube tends to shrink, possibly due to capillary force during drying. Reaction for a longer time (e.g., 10 min) completely consumes MnO_2, producing pure PANI nanotubes (Figures 2d and S4). The long PANI nanotubes in electron microscopy images exhibit bent geometries (Figure S5), different from the straight geometry of the MnO_2 nanotubes, confirming the mechanical flexibility of PANI.

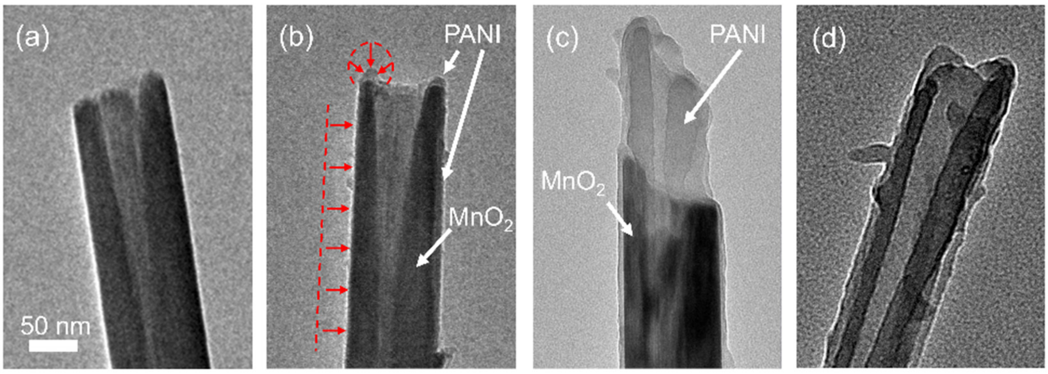

Figure 2. Typical TEM images of representative α-MnO_2 nanotube (**a**) and (**b**–**d**) after reaction with aniline for different times: (**b**) 1 min, (**c**) 5 min, and (**d**) 10 min. The dotted curve and line in (**b**) indicate the diffusion cross-sections of aniline toward the end and side surface, respectively. The red arrows indicate the diffusion direction of aniline.

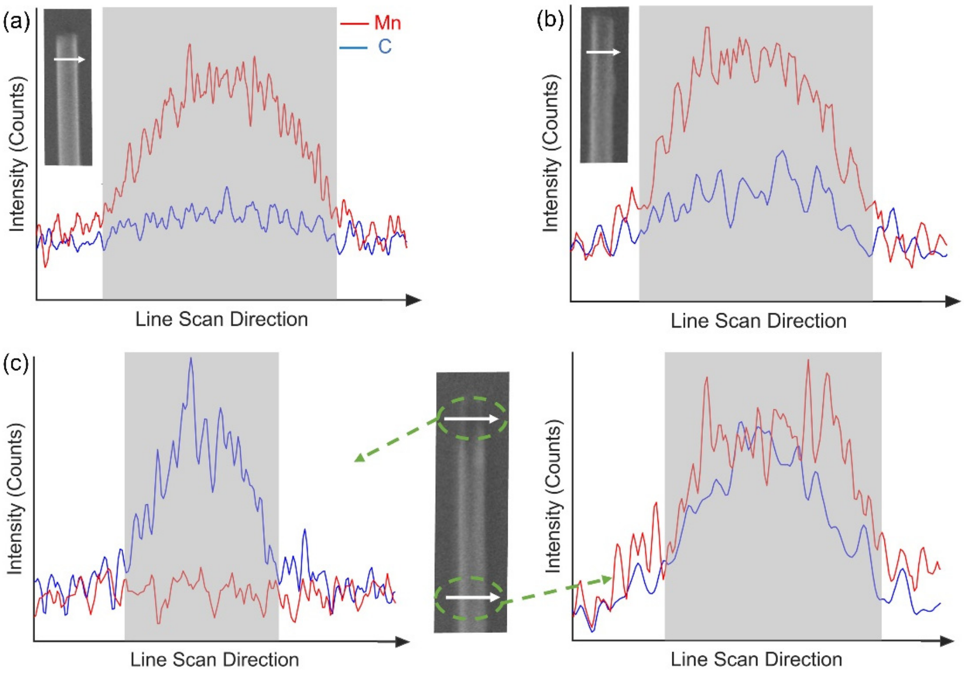

Figure 3. Line-scan EDS profiles of Mn and C along individual nanotubes before (**a**) and after (**b**,**c**) the α-MnO_2 nanotubes react with aniline for different times: (**b**) 1min. and (**c**) 10 min. The insets are the nanotubes that have

been studied. The arrows highlight the positions for EDS analysis and line-scan directions. The grey boxes highlight the edges of the studied nanotubes, which determine their lateral dimensions.

The Fourier transform infrared (FTIR) spectrum of the as-synthesized nanotubes exhibits characteristic peaks of PANI (Figure S6). The two peaks located at 1583 cm^{-1} and 1498 cm^{-1} are attributed to quinonoid and benzenoid ring stretching respectively [24]. The weak peak at 1384 cm^{-1} appears as a result of C-N stretching of alternating quinonoid-benzenoid-quinonoid rings within the PANI structure [25]. The peak at 1315 cm^{-1} represents the C-N vibrational mode of secondary aromatic amines [26] while the peak at 1267 cm^{-1} is attributed to the polaron lattice C-N stretching mode [27]. The broad peak at 1142 cm^{-1} is associated with positively charged $-NH^+$ stretching modes within the polymer arising from the high degree of polymer backbone protonation while the peak at 699 cm^{-1} represents -NH wagging in secondary amines. The peak at 824 cm^{-1} corresponds to the out of plane C-H stretching modes of para-disubstituted benzene rings arising from the end to end monomer coupling during the polymerization reaction [25].

The color evolution of the solution during the conversion of MnO_2 nanotubes to PANI nanotubes allows using ultraviolet (UV)-visible absorption spectroscopy to follow the redox/polymerization reactions on MnO_2 surfaces. The emeraldine PANI phase has three characteristic absorption bands in the UV-visible spectral range. According to the previous studies on emeraldine PANI films [28], the absorption band around 4 eV (or 310 nm) originates from the π-π^* transition, owing to the excitation of benzenoid rings within the polymer chain. This transition is present in both aniline monomer and PANI of all phases. The emeraldine base has an absorption band at ~2.1 eV (or 590 nm) due to the localized benzenoid HOMO (highest occupied molecular orbital) to quinoid LUMO (lowest unoccupied molecular orbital) excitation. Protonation of the emeraldine base leads to the formation of bipolarons, in which the two N atoms connecting to the quinoid rings are protonated with positive charges. Such localized protonation could elevate the quinoid LUMO position and blueshift the absorption band. The internal redox reaction of bipolarons transforms quinoids into benzenoid rings, forming polarons. The following polaron separation spreads the polarons to form a polaronic lattice with alternated cations $(-{}_{+}\overset{:}{\mathrm{N}}\mathrm{H}-)$ along the polymer chains. The polymer chain with high-density polarons possesses a polaron band that is half occupied with electrons. Excitation of electrons from the fully occupied lower-energy band to the polaron band becomes possible, shifting the HOMO-LOMO absorption peak to the red around 1.5 eV (or 825 nm). The polaron band transition usually gives an intense and broad absorption peak. Further protonation increases the density of polarons to exhibit polaron bications that are neighboring polarons. Such breaking of the polaron lattice makes the emeraldine PANI more metallic, extending its absorption further to the near-infrared region [28,29].

Figure 4 plots the time-dependent UV-visible extinction spectra of an acidic dispersion of MnO_2 nanotubes before and after the reaction with aniline for different times. The extinction spectrum of the MnO_2 nanotubes shows a shallow and broad peak at 610 nm (black curve, Figure 4a). The significant baseline offset is attributed to the strong scattering of the MnO_2 nanotubes due to their longitudinal dimensions comparable to or larger than the light wavelength. The dispersion of the MnO_2 nanotubes is opaque (inset, Figure S3), confirming the strong scattering of the nanotubes. Once the reaction with aniline starts, a strong absorption peak at 530 nm and a weak shoulder peak at 700 nm emerge simultaneously (see the spectrum at 15 s), indicating the formation of protonated emeraldine PANI dominated by bipolarons. The absorption peak of MnO_2 is too weak to display and be embedded in the strong absorption of PANI. The absorption of resulting Mn^{2+} cations is also very weak compared to PANI (Figure S7). Therefore, the peaks observed in the extinction spectra are dominated by the absorption of emeraldine PANI. As the reaction continues, the peak at the shorter wavelength slightly increases and redshifts. The peak at the longer wavelength significantly increases in intensity, but its position remains unchanged. The evolution of these two absorption peaks indicates that thicker PANI favors the formation of polaron lattice at longer reaction times. For example, the PANI nanotubes formed at 10 min after complete consumption of MnO_2 essentially exhibit one peak at 700 nm (yellow curve, Figure 4a), indicating the freshly produced PANI nanotubes are composed of polymer chains primarily with polaron lattices. This extinction spectrum still shows a large offset baseline without the MnO_2 nanotubes, indicating that the resulting PANI nanotubes have strong scattering. The strong scattering makes the dispersion of PANI nanotubes opaque (inset, Figure S5). In contrast, the PANI dispersion synthesized using APS exhibits an extinction spectrum with a smaller offset (Figure S8), indicating that the lateral dimensions of the PANI nanostructures are smaller compared to the PANI nanotubes. The PANI product is dominated by wavy and entangled nanofibers with thin diameters, which could be easily swollen with solvent to minimize the difference in dielectric constant between the PANI nanofibers and solvent. Both the small lateral dimensions and swelling of the PANI nanofibers lower their optical scattering. The PANI synthesized from reaction with polycrystalline MnO_2 shells with rough surfaces [19] gives a transparent solution even though the spherical MnO_2 shells have sizes over 2 μm (Figure S9). The lack of strong light scattering implies that the resulting PANI cannot inherit the geometry and dimension from the polycrystalline MnO_2 shells but form fragments. The differences in PANI products formed from the reactions with the single-crystalline MnO_2 nanotubes and the polycrystalline MnO_2 shells confirm the importance of single crystallinity, which prevents the reactive MnO_2 from falling apart during reaction with aniline, and smooth surface, which provides the solid/liquid interface favoring the localized polymerization and growth of PANI against the MnO_2 surface, in synthesizing PANI nanotubes that can inherit the geometry and dimensions of the MnO_2 nanotubes.

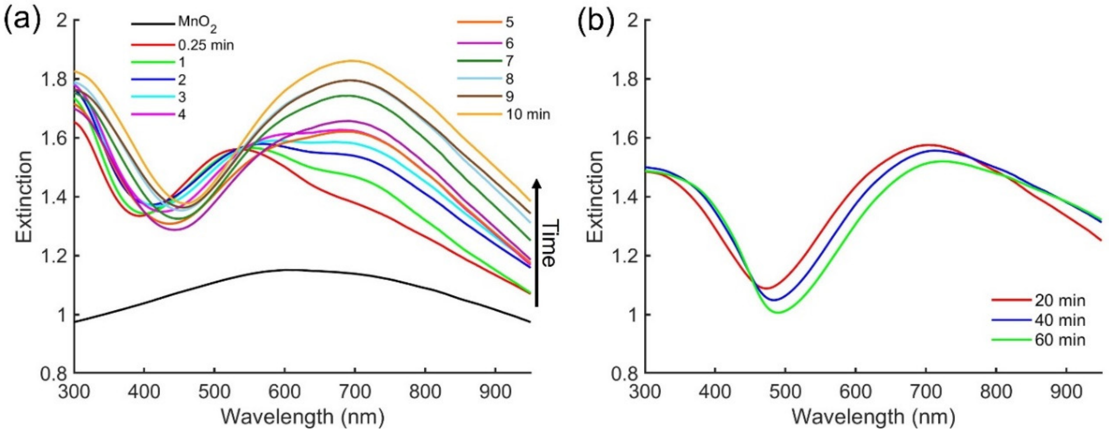

Figure 4. Time-dependent UV-Visible extinction spectra of the dispersion of MnO_2 nanotubes before (black curve) and after reaction with aniline for different times: (**a**) 15 s–10 min and (**b**) 20 min–60 min. Note: The first spectrum (red curve) in (**a**) was recorded at 15 s (i.e., 0.25 min), the second spectrum (green curve) was recorded at 1 min, and the following spectra were collected at an interval of 1 min. The units of the legends in (**a**) are the same as min.

Since the absorption peaks at 530 nm and 700 nm originated from the emeraldine PANI, it is feasible to use their intensity to roughly estimate the extent of polymerization, which is approximately proportional to the absorbance [30]. The integrated area by using the line connecting the peak valley around 400 nm and the data point at the longest wavelength (i.e., 980 nm) as the baseline is used to evaluate the polymerization kinetics during the reaction of aniline with the MnO_2 nanotubes (Figure S10). The integrated area exhibits a linear dependence on the reaction time at the middle stage of the reaction (i.e., 2–7 min), indicating that the polymerization follows a quai-zeroth reaction order and is independent of concentrations of both aniline and MnO_2 nanotubes. Such concentration independence indicates that the exposed MnO_2 surfaces (i.e., the end surfaces with an almost constant value) primarily determine the reaction kinetics when the diffusion of aniline does not limit the reaction. The polymerization becomes slower at the late stage (Figure S10), where the concentration of aniline is so low that diffusion starts limiting the reaction. After the complete redox and polymerization reaction, incubating the PANI nanotubes in the acidic reaction solution leads to a slight decrease in peak intensity at 700 nm and an overall broadband increase in the near-infrared region (Figure 4b). The soaking allows deep protonation of the polaron lattices (alternated polaron distribution along polymer chains) to polymer chains with high-density polarons (i.e., forming neighboring polaron bications), making PANI more metallic (or conductive) to extend its optical absorption to even longer wavelength, i.e., near-infrared region [31].

The transformation of transient template MnO_2 nanotubes to PANI nanotubes through an interfacial redox reaction provides a possibility to form PANI nanotubes coated with an inorganic layer, which is difficult to deposit on PANI directly. For example, the conventional sol-gel process cannot grow a silica coating on PANI nanostructures through controlled hydrolysis of tetraethyl orthosilicate (TEOS) in the presence of the PANI nanostructures in a solution due to the chemical non-wettability between silica and PANI. In contrast, it is convenient to grow a silica layer on MnO_2 nanotubes, forming MnO_2@silica core-shell nanotubes, through the sol-gel process [32]. When the silica coating is thin enough (<20 nm), the intrinsic porosity of the thin silica layer still allows the diffusion of aniline molecules to react with MnO_2 nanotubes and outward diffusion of Mn^{2+} ions, resulting in the transformation of the MnO_2 nanotubes into PANI ones inside the silica shells (Figure 5). The FTIR spectrum of the resulting composite nanotubes exhibits the same characteristic peaks of the PANI nanotubes shown in Figure 2d, confirming the conversion of MnO_2 to PANI (Figure S6). The formation of PANI nanotubes inside the silica shells indicates the diffusion of aniline monomer accross the silica layer. The EDS linescan profiles of Si (corresponding to silica shell) and C (corresponding to PANI tube) of a single composite tube (Figure S11) show that the signal of Si is wider than the signal of C, highlight the PANI@silica core-shell structure. The lack of Mn signal and strong C signal indicate the complete reaction of MnO_2 with aniline monomers to yielding soluble

Mn^{2+} ions and PANI core tubes. Due to the versatile chemistry of silica, the presence of silica layer outside the PANI nanotubes enables the feasibility to modify or graft interesting components onto the composite nanotubes, adding appropriate properties/functionalities to the PANI nanotubes.

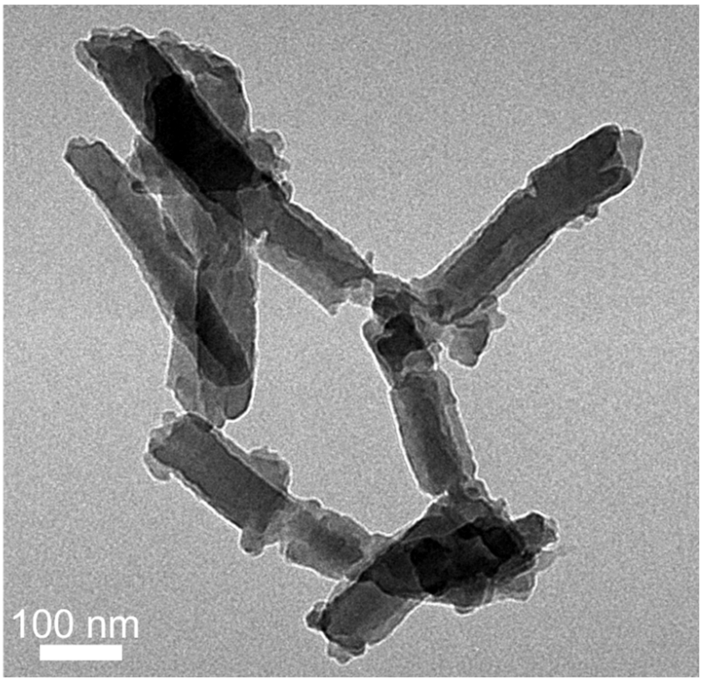

Figure 5. Typical TEM image of representative PANI@silica nanotubes.

4. Conclusion

Single-crystalline α-phase MnO_2 nanotubes have been used as a new class of solid-state oxidant to oxidize aniline and promote polymerization of emeraldine PANI in the appropriate acidic solutions. The MnO_2 nanotubes with smooth surfaces also serve as transient templates to confine the polymerization against the MnO_2 surfaces, forming pure PANI nanotubes with dimensions determined by the MnO_2 nanotubes and reaction stoichiometry. The reduction of MnO_2 into soluble Mn^{2+} ions is also crucial for hollow PANI nanostructures, which inherit the geometry of MnO_2 nanostructures. The reaction of aniline with CeO_2 nanoparticles failed to produce hollow PANI shells because Ce_2O_3 (i.e., the product of reduced CeO_2) is not soluble. After the initial reaction, the presence of thin Ce_2O_3 coating on CeO_2 prevents the contact between aniline and CeO_2, thus ceasing the continuous redox reaction. This work shed light on using highly crystalline reactive oxide nanostructures as transient templates to synthesize shape-controlled conducting polymer nanostructures through oxidation-induced polymerization.

Supplementary Materials: The following supporting information can be downloaded at: https://www.sciltp.com/journals/mi/2024/1/578/s1, Figure S1. Change of solution pH value as aniline added to the dispersion of MnO_2 nanostructures at 30, 90, 180, 270 s. The jump of pH value indicates the consumption of protons as aniline being oxidized by MnO_2. Figure S2. XRD pattern of the synthesized MnO_2 nanotubes. Figure S3. (a) Scanning electron microscopy (SEM) image of the synthesized MnO_2 nanotubes. The nanotubes standing out-of-substrate show the square cross sections and hollow interiors. The inset is a photo of an aqueous dispersion of the MnO_2 nanotubes. (b) Statistic histogram of the lateral dimensions of individual MnO_2 nanotubes. Figure S4. Line-scan EDS profiles across a PANI nanotube (formed from 10-minute reaction as shown in Figure 2d) at different locations. The near-zero signals of Mn regardless of position confirm the complete consumption of MnO_2 throughout the entire nanotube. The gray boxes highlight the boundaries of the nanotube along the scan traces. Figure S5. Transmission electron microscopy (TEM) image of the synthesized PANI nanotubes. The bended curves along their longitudinal directions indicate their mechanical flexibility. Figure S6. FTIR spectrum of the as-synthesized PANI nanotubes as shown in Figure 2d and PANI@silica nanotubes as shown in Figure 5. Figure S7. Absorption spectrum of the supernatant after complete reaction of the MnO_2 nanotubes. The absorbance beyond 500 nm, where optical absorption of the emeraldine PANI locates, is lower than 0.01, which is less than 2% of the peak absorption of the PANI nanotube dispersion. Therefore, it is reasonable to ignore the influence of resulting Mn^{2+} on the extinction spectra during the reaction. Figure S8. (a) TEM image of PANI synthesized using APS. The inset is the photo of the PANI dispersion. (b) Extinction spectrum of the PANI dispersion. The concentration of aniline units is same as that used in the synthesis of PANI nanotubes. Figure S9. (a) SEM image of MnO_2 spherical shells with rough surfaces. (b) TEM image of PANI synthesized from reaction with the MnO_2 shells. The inset is the photo of the PANI dispersion. (c) Extinction spectrum of the PANI dispersion. The concentration of aniline units is same as that used in the synthesis of PANI nanotubes. Figure S10. Time-dependent integrated area of the absorption beyond the valley points in Figure 4a. The integration was processed using the line connecting the valley point around 400 nm and the data point at the longest wavelength (i.e., 980 nm) in each spectrum. Figure S11. Line-scan EDS profiles of a synthesized PANI@silica core-shell nanotube. The inset represents the SEM image of the PANI@silica nanotube, with an arrow highlighting the scan position and direction. The grey box represents the outer boundary of the nanotube along the scan traces. Table S1: Reactivity of MnO_2 nanotubes and the resulting PANI phase at different pH of reaction solution.

Author Contributions: D.K. and Y.S. conceptualized the project. Z.Z., D.K. and Y.S. supervised the project. M.S. and G.P. conducted the experiment. All authors discussed and analyzed the results. M.S. drafted the manuscript, and all authors contributed to revising it. All authors have read and agreed to the published version of manuscript.

Funding: This work was supported through the subcontract No. SciTech 22-22-F-0037-02 funded by US Army DEVCOM Chemical Biological Center. Materials characterization was partially performed at Temple Materials Institute.

Data Availability Statement: The data that support the findings of this study are available from the corresponding authors upon reasonable request.

Conflicts of Interest: The authors declare no conflict of financial interest.

References

1. McQuade, D.T.; Pullen, A.E.; Swager, T.M. Conjugated Polymer-Based Chemical Sensors. *Chem. Rev.* **2000**, *100*, 2537–2574. https://doi.org/10.1021/cr9801014.
2. Yang, D.; Wang, J.; Cao, Y.; Tong, X.; Hua, T.; Qin, R.; Shao, Y. Polyaniline-Based Biological and Chemical Sensors: Sensing Mechanism, Configuration Design, and Perspective. *ACS Appl. Electron. Mater.* **2023**, *5*, 593–611. https://doi.org/10.1021/acsaelm.2c01405.
3. Novák, P.; Müller, K.; Santhanam, K.S.V.; Haas, O. Electrochemically Active Polymers for Rechargeable Batteries. *Chem. Rev.* **1997**, *97*, 207–282. https://doi.org/10.1021/cr941181o.
4. Wang, K.; Wu, H.; Meng, Y.; Wei, Z. Conducting Polymer Nanowire Arrays for High Performance Supercapacitors. *Small* **2014**, *10*, 14–31. https://doi.org/10.1002/smll.201301991.
5. Zare, E.N.; Makvandi, P.; Ashtari, B.; Rossi, F.; Motahari, A.; Perale, G. Progress in Conductive Polyaniline-Based Nanocomposites for Biomedical Applications: A Review. *J. Med. Chem.* **2020**, *63*, 1–22. https://doi.org/10.1021/acs.jmedchem.9b00803.
6. Tran, H.D.; D'Arcy, J.M.; Wang, Y.; Beltramo, P.J.; Strong, V.A.; Kaner, R.B. The Oxidation of Aniline to Produce "Polyaniline": A Process Yielding Many Different Nanoscale Structures. *J. Mater. Chem.* **2011**, *21*, 3534–3550. https://doi.org/10.1039/C0JM02699A.
7. Sapurina, I.; Stejskal, J. The Mechanism of the Oxidative Polymerization of Aniline and the Formation of Supramolecular Polyaniline Structures. *Polym. Int.* **2008**, *57*, 1295–1325. https://doi.org/10.1002/pi.2476.
8. Pavitt, A.S.; Bylaska, E.J.; Tratnyek, P.G. Oxidation Potentials of Phenols and Anilines: Correlation Analysis of Electrochemical and Theoretical Values. *Environ. Sci. Process. Impacts* **2017**, *19*, 339–349. https://doi.org/10.1039/C6EM00694A.
9. Zhang, X.; Manohar, S.K. Polyaniline Nanofibers: Chemical Synthesis Using Surfactants. *Chem. Commun.* **2004**, *20*, 2360. https://doi.org/10.1039/b409309g.
10. Kim, B.-J.; Oh, S.-G.; Han, M.-G.; Im, S.-S. Preparation of Polyaniline Nanoparticles in Micellar Solutions as Polymerization Medium. *Langmuir* **2000**, *16*, 5841–5845. https://doi.org/10.1021/la9915320.
11. Wei, Z.; Zhang, Z.; Wan, M. Formation Mechanism of Self-Assembled Polyaniline Micro/Nanotubes. *Langmuir* **2002**, *18*, 917–921. https://doi.org/10.1021/la0155799.
12. Wu, C.-G.; Bein, T. Conducting Polyaniline Filaments in a Mesoporous Channel Host. *Science* **1994**, *264*, 1757–1759. https://doi.org/10.1126/science.264.5166.1757.
13. Pan, L.J.; Pu, L.; Shi, Y.; Song, S.Y.; Xu, Z.; Zhang, R.; Zheng, Y.D. Synthesis of Polyaniline Nanotubes with a Reactive Template of Manganese Oxide. *Adv. Mater.* **2007**, *19*, 461–464. https://doi.org/10.1002/adma.200602073.
14. Han, J.; Wang, M.; Cao, S.; Fang, P.; Lu, S.; Chen, R.; Guo, R. Reactive Template Strategy for Fabrication of MnO_2/Polyaniline Coaxial Nanocables and Their Catalytic Application in the Oxidative Decolorization of Rhodamine B. *J. Mater. Chem. A* **2013**, *1*, 13197–13202. https://doi.org/10.1039/C3TA12545A.
15. Ren, L.; Zhang, G.; Wang, J.; Kang, L.; Lei, Z.; Liu, Z.; Liu, Z.; Hao, Z.; Liu, Z. Adsorption–Template Preparation of Polyanilines with Different Morphologies and Their Capacitance. *Electrochim. Acta* **2014**, *145*, 99–108. https://doi.org/10.1016/j.electacta.2014.08.088.
16. Tian, Y.; Li, H.; Liu, Y.; Cui, G.; Sun, Z.; Yan, S. Morphology-Dependent Enhancement of Template-Guided Tunable Polyaniline Nanostructures for the Removal of Cr(VI). *RSC Adv.* **2016**, *6*, 10478–10486. https://doi.org/10.1039/C5RA25630E.
17. Han, J.; Li, L.; Fang, P.; Guo, R. Ultrathin MnO_2 Nanorods on Conducting Polymer Nanofibers as a New Class of Hierarchical Nanostructures for High-Performance Supercapacitors. *J. Phys. Chem. C* **2012**, *116*, 15900–15907. https://doi.org/10.1021/jp303324x.
18. Feng, X.; Zhang, Y.; Yan, Z.; Chen, N.; Ma, Y.; Liu, X.; Yang, X.; Hou, W. Self-Degradable Template Synthesis of Polyaniline Nanotubes and Their High Performance in the Detection of Dopamine. *J. Mater. Chem. A* **2013**, *1*, 9775–9780. https://doi.org/10.1039/C3TA11856H.

19. Fei, J.; Cui, Y.; Yan, X.; Yang, Y.; Wang, K.; Li, J. Controlled Fabrication of Polyaniline Spherical and Cubic Shells with Hierarchical Nanostructures. *ACS Nano* **2009**, *3*, 3714–3718. https://doi.org/10.1021/nn900921v.
20. Li, X.; Liu, X.; Qiao, X.; Xing, S. Confining the Polymerization of Aniline to Generate Yolk–Shell polyaniline@SiO_2 Nanostructures. *RSC Adv.* **2015**, *5*, 79172–79177. https://doi.org/10.1039/C5RA15065E.
21. Truong, T.T.; Liu, Y.; Ren, Y.; Trahey, L.; Sun, Y. Morphological and Crystalline Evolution of Nanostructured MnO_2 and Its Application in Lithium–Air Batteries. *ACS Nano* **2012**, *6*, 8067–8077. https://doi.org/10.1021/nn302654p.
22. Xiao, W.; Wang, D.; Lou, X.W. Shape-Controlled Synthesis of MnO_2 Nanostructures with Enhanced Electrocatalytic Activity for Oxygen Reduction. *J. Phys. Chem. C* **2010**, *114*, 1694–1700. https://doi.org/10.1021/jp909386d.
23. Sun, Y.; Xia, Y. Mechanistic Study on the Replacement Reaction between Silver Nanostructures and Chloroauric Acid in Aqueous Medium. *J. Am. Chem. Soc.* **2004**, *126*, 3892–3901. https://doi.org/10.1021/ja039734c.
24. Furukawa, Y.; Ueda, F.; Hyodo, Y.; Harada, I.; Nakajima, T.; Kawagoe, T. Vibrational Spectra and Structure of Polyaniline. *Macromolecules* **1988**, *21*, 1297–1305. https://doi.org/10.1021/ma00183a020.
25. Trchová, M.; Stejskal, J. Polyaniline: The Infrared Spectroscopy of Conducting Polymer Nanotubes (IUPAC Technical Report). *Pure Appl. Chem.* **2011**, *83*, 1803–1817. https://doi.org/10.1351/PAC-REP-10-02-01.
26. Boyer, M.-I.; Quillard, S.; Rebourt, E.; Louarn, G.; Buisson, J.P.; Monkman, A.; Lefrant, S. Vibrational Analysis of Polyaniline: A Model Compound Approach. *J. Phys. Chem. B* **1998**, *102*, 7382–7392. https://doi.org/10.1021/jp972652o.
27. Boyer, M.I.; Quillard, S.; Louarn, G.; Froyer, G.; Lefrant, S. Vibrational Study of the $FeCl_3$-Doped Dimer of Polyaniline; A Good Model Compound of Emeraldine Salt. *J. Phys. Chem. B* **2000**, *104*, 8952–8961. https://doi.org/10.1021/jp000946v.
28. Huang, W.S.; MacDiarmid, A.G. Optical Properties of Polyaniline. *Polymer* **1993**, *34*, 1833–1845. https://doi.org/10.1016/0032-3861(93)90424-9.
29. Stafström, S.; Brédas, J.L.; Epstein, A.J.; Woo, H.S.; Tanner, D.B.; Huang, W.S.; MacDiarmid, A.G. Polaron Lattice in Highly Conducting Polyaniline: Theoretical and Optical Studies. *Phys. Rev. Lett.* **1987**, *59*, 1464–1467. https://doi.org/10.1103/PhysRevLett.59.1464.
30. Neoh, K.G.; Kang, E.T.; Tan, K.L. Evolution of Polyaniline Structure during Synthesis. *Polymer* **1993**, *34*, 3921–3928. https://doi.org/10.1016/0032-3861(93)90521-B.
31. Canales, M.; Torras, J.; Fabregat, G.; Meneguzzi, A.; Alemán, C. Polyaniline Emeraldine Salt in the Amorphous Solid State: Polaron versus Bipolaron. *J. Phys. Chem. B* **2014**, *118*, 11552–11562. https://doi.org/10.1021/jp5067583.
32. Shi, X.; Cao, M.; Fang, X. β-MnO_2/SiO_2 Core–Shell Nanorods: Synthesis and Dielectric Properties. *J. Nanosci. Nanotechnol.* **2011**, *11*, 6953–6958. https://doi.org/10.1166/jnn.2011.4252.